ROYAL SOCIETY OF CHEMISTRY

Journal Name

ARTICLE

Plasmonic circular dichroism of vesicle-like nanostructures by template-less self-assembly of achiral Janus nanoparticles

Received 00th January 20xx, Accepted 00th January 20xx

DOI: 10.1039/x0xx00000x

www.rsc.org/

Jia En Lu^a, Chou-Hsun Yang^b, Haobin Wang^b, ChiYung Yam^c, Zhi-Gang Yu^{d,*}, and Shaowei Chen^{a,*}

Chiral nanostructures have been attracting extensive interest in recent years primarily because of the unique materials properties that can be exploited for diverse applications. In this study, gold Janus nanoparticles, with hexanethiolates and 3-mercapto-1,2-propanediol segregated on the two hemispheres of the metal cores (dia. 2.7 ± 0.4 nm), self-assembled into vesicle-like, hollow nanostructures in both water or organic media, and exhibited apparent plasmonic circular dichroism (PCD) absorption in the visible range. This was in contrast to individual Janus nanoparticles, bulk-exchange nanoparticles where the two ligands were homogeneously mixed on the nanoparticle surface, or nanoparticles capped with only one kind of the ligands. The PCD signals were found to become intensified with increasing coverage of the 3-mercapto-1,2-propanediol ligands on the nanoparticle surface. This was accounted for by the dipolar property of the structurally asymmetrical Janus nanoparticles, and theoretical simulations based on first principles calculations showed that when the nanoparticle dipoles self-assembled onto the surface of a hollow sphere, a vortex was formed which gave rise to the unique chiral characteristics. The resulting chiral nanoparticle vesicles could be exploited for the separation of optical enantiomers, as manifested in the selective identification and separation of D-alanine from the L-isomer

1. Introduction

In recent years, plasmonic metal nanoparticles have been found to exhibit unique chiroptical properties, and the nanoscale chirality may be exploited for enantiomeric sensing and catalysis, as well as development of next-generation optoelectronic devices. 1-3 Unlike conventional chiral molecules (e.g., peptides, proteins, and DNA) that typically exhibit circular dichroism (CD) absorption in the far ultraviolet (UV, 140 - 250 nm) region,4,5 plasmonic circular dichroism (PCD) is generally observed in the visible range and can be readily manipulated by the chemical nature and morphology of the plasmonic nanoparticles.² This may be due to the formation of intrinsically chiral nanoparticle cores, capping with chiral organic ligands, as well as arrangements of achiral nanoparticles into chiral organized ensembles. In the first strategy, chiral templates are generally used to assist the growth of nanoparticles, where chirality is imprinted onto the nanoparticle core during the growth process, resulting in the formation of chiral nanoparticles.⁶ For instance, Shemer et al.⁷ demonstrated that chirality could be inherited by silver nanoparticles using DNA as templates during nanoparticle formation, whereas silver nanoparticles that were prepared by NaBH₄ reduction and then underwent ligand exchange reactions with the same DNA ligands did not show any CD signal in the same wavelength region. The intrinsic chirality of plasmonic nanoparticles can also arise from a chiral core shape, such as helical/spiral structures and/or the formation of chiral microfacets on the nanoparticle surfaces.8-12 For achiral plasmonic nanoparticles, PCD can also be produced by using chiral capping ligands, due to strong dipole (and higher-order) interactions between the ligand and nanoparticle core electrons. Upon interactions with the chiral ligands, the symmetry of the electronic property on the nanoparticle surface is distorted, leading to different extinction coefficients between the left- and right-handed circularly polarized light. 13-15 For instance, L-glutathione-capped gold nanoparticles¹⁶ and silver nanocubes¹⁷ have been found to exhibit well-defined PCD signals that coincide with the surface plasmon resonance (SPR) absorption of the nanoparticles. PCD has also been observed with chiral molecules entrapped at the core-shell interface of Au@Ag nanorods.18

Nanoscale chirality can also be induced by controlled assembly of nanoparticles into chiral superstructures. ¹⁹ For instance, PCD has been observed with gold nanoparticle networks formed by using (chiral) DNA or peptides as interparticle linkers, ^{20, 21} arrangements of gold nanoparticles onto helical nanofiber templates, ²²⁻²⁴ and layer-by-layer deposition of gold nanoparticles into twisted chains. ²⁵ Plasmonic chiroptical properties have also been found with heterodimers of two gold nanoparticles of different sizes (50 nm and 150 nm) due to the interference between the higher-

^a Department of Chemistry and Biochemistry, University of California, 1156 High Street, Santa Cruz, California 95064, USA. E-mail: shaowei@ucsc.edu

b. Department of Chemistry, University of Colorado Denver, Denver, Colorado 80217, USA

German Science Research Center, Haidian District, Beijing 100193, China

d-Institute for Shock Physics and Department of Physics and Astronomy, Washington State University, Pullman, Washington 99164, USA. E-mail: zhigang.yu@wsu.edu

[†] Footnotes relating to the title and/or authors should appear here. Electronic Supplementary Information (ESI) available: TEM, NMR, FTIR, AFM, UV-vis, CD, and computational data. See DOI: 10.1039/x0xx00000x

order and dipolar modes in the heterodimer pair,²⁶ as well as three-dimensional oligomers of gold nanorods.²⁷⁻²⁹

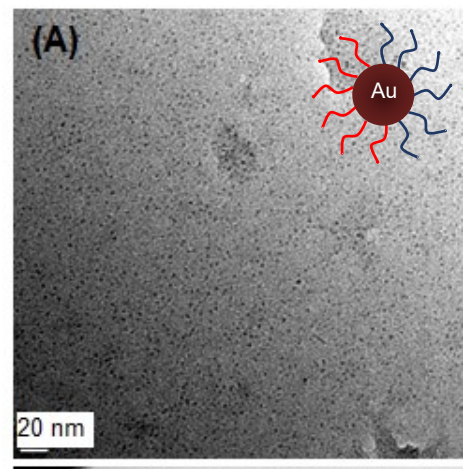
In the present study, we demonstrated that gold Janus nanoparticles (JNPs), with hydrophobic hexanethiolates (C6) and hydrophilic 3-mercapto-1,2-propanediol (MPD) ligands segregated on the two hemispheres of the metal cores, selfassembled into vesicle-like, hollow nanostructures without the assistance of any chiral templates/scaffolds, and exhibited apparent PCD absorption in the visible range. This was accounted for by the dipolar property of the structurally asymmetrical JNPs arranged on a hollow sphere forming a vortex, as manifested in theoretical simulations based on first principles calculations, in sharp contrast with the achiral response observed with individual JNPs, bulk-exchange nanoparticles with the two ligands homogeneously mixed on the nanoparticle surface, or nanoparticles capped with only one kind of the ligands. The unique chiral characteristics of the JNP vesicles can be exploited for selective binding and phase transfer of optical enantiomers, as manifested in the effective identification and separation of D-alanine from the L-isomer.

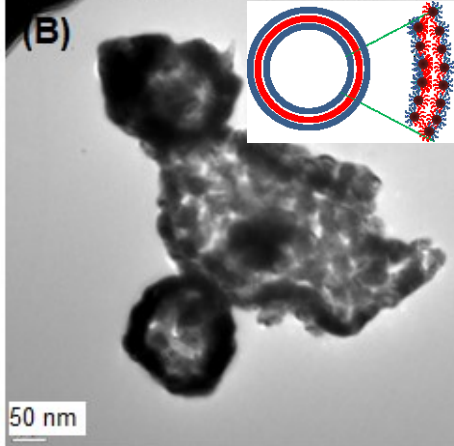
2. Results and discussion

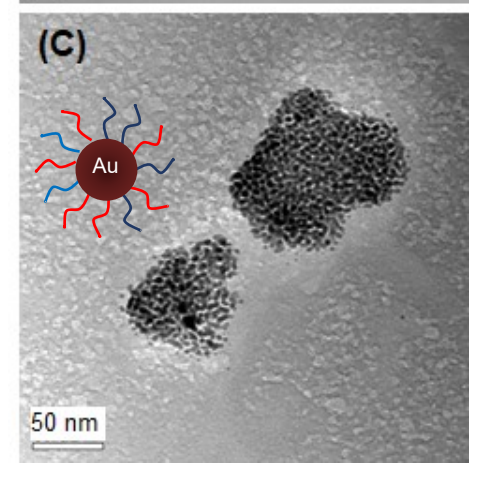
As described previously (and detailed in the Experimental Section),30-32 the JNPs were prepared by interfacial ligand exchange reactions of hexanethiolate-capped gold (AuC6, 2.7 \pm 0.4 nm in diameter, Figure S1) nanoparticles with (racemic) MPD at the air water interface, exhibiting hydrophobic C6 ligands on one face and hydrophilic MPD on the other (inset to Figure 1A).33 The surface concentration of MPD was varied by reaction time (1, 4, and 10 h), and quantitatively evaluated by ¹H NMR measurements at 17.5 % for JNP1, 28.3 % for JNP4, and 61.4 % for JNP10, based on the integrated peak areas of the terminal methyl protons of the C6 ligands and the methoxy protons of the MPD ligands (Figure S2).30 For the control sample where the ligand exchange reaction was carried out by simply mixing AuC6 and MPD in THF (BE nanoparticles, inset to Figure **1C**), the MPD surface coverage was estimated to be ca. 66.0%. That is, the JNP10 and BE nanoparticles are akin to structural isomers with a similar core-ligand composition but a different surface distribution of the capping ligands. The incorporation of MPD ligands onto the nanoparticle surfaces was also manifested in FTIR measurements (Figure S3), where the O-H stretch can be found at 3300 - 3200 cm⁻¹ and the C-O vibration at 1030 cm⁻¹.30

JNPs have been known to behave analogously to amphiphilic surfactant molecules, and can self-assemble into organized vesicle-like superstructures both in water and apolar organic solvents such as THF and CHCl₃.^{32, 34} In fact, in an earlier study,³⁴ the critical micelle concentration (CMC) of JNPs was found to be at least three orders of magnitude lower than that of Triton X-100. Such concentration dependence of the formation of nanoparticle ensembles can be visually evidenced in TEM measurements. From **Figure 1A**, one can see that at the concentration of 0.01 mg/mL in water, JNP10 nanoparticles were well dispersed as individual particles without apparent agglomeration. Yet when the concentration was increased to

0.15 mg/mL, the nanoparticles can be seen to form vesicle-like, hollow organized assemblies with lateral dimensions in the range of 50 to 200 nm (Figure 1B and inset, and Figure S1).³² The variation of the nanoparticle morphologies can also be manifested in AFM topographic measurements (Figure S4). One may notice that whereas BE nanoparticles also formed ensemble structures of similar dimensions (Figure 1C and S1), the nanoparticle superstructures are solid rather than hollow. This may be due to the segregated distribution of the (hydrophobic) C6 and (hydrophilic) MPD ligands on the JNP surface that rendered it possible for the nanoparticles to arrange into vesicle-like structures, whereas for the BE nanoparticles, the random mix of the C6 and MPD ligands made







2 | *J. Name.*, 2012, **00**, 1-3

This journal is © The Royal Society of Chemistry 20xx

it difficult for the nanoparticles to find an orientation with a minimal surface energy.

Figure 1. TEM images of JNP10 at a concentration of (A) 0.01 mg/mL and (B) 0.15 mg/mL in water. (C) BE nanoparticles at 0.15 mg/mL in water. Scale bars are 20 nm in panel (A), and 50 nm in panels (B) and (C). Insets are the schematic illustrations of (A) JNP, (B) JNP assembly, and (C) BE nanoparticles.

The optical properties of the nanoparticles were then examined by UV-vis absorption measurements. **Figure 2A** depicts the UV-vis spectra of the series of JNP and BE nanoparticles in water at the concentration of 0.15 mg/mL. One can see that at this concentration, both JNP (black, red, and green curves) and BE nanoparticles (yellow curve) showed a broad absorption peak at ca. 610 nm, a marked red-shift of ca. 100 nm as compared to the SPR of the original AuC6 nanoparticles in CHCl₃ (**Figure S5**) and AuMPD nanoparticles (blue curve) that were readily dispersed in water, due to strong interparticle electronic interactions as a result of the formation of nanoparticle ensembles (Figure 1B). ^{35, 36}

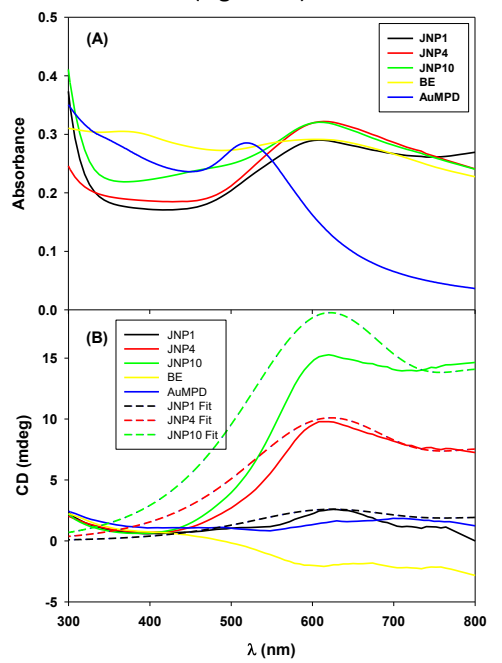


Figure 2. (A) UV-vis and (B) CD spectra of JNP, BE and AuMPD nanoparticles at a concentration of 0.15 mg/mL in water. Dashed curves in (B) are the fitting CD spectra of a hollow sphere (dia. 50 nm) consisting of Janus nanoparticles (core dia. 1.6 nm) by eq. (17).

Interestingly, the three JNP ensembles all exhibited apparent PCD signals at wavelength greater than 500 nm (Figure 2B), with the intensity maxima matching the corresponding SPR peaks (Figure 2A), and the PCD intensity increased with increasing MPD coverage on the nanoparticle surface, +2.6 mdeg for JNP1, +9.9 mdeg for JNP4 and +15.2 mdeg for JNP10. This result indicates that increasing dissymmetry of the distribution of surface capping ligands facilitates the formation of vesicle-like, hollow nanostructures that are PCD-active. By contrast, BE nanoparticles, exhibited only a weak PCD signal (ca. –2.05 mdeg), despite a ligand composition and SPR absorption similar to that of JNP10, suggesting that solid ensembles of the nanoparticles were PCD-inactive. This also suggests minimal contributions from the (racemic) MPD ligands to the PCD signals of the JNPs, as control

experiment with AuMPD nanoparticles exhibited virtually no PCD signals.

Furthermore, one can see that the PCD intensity of the JNP samples varied with nanoparticle concentration. As noted earlier, formation of nanoparticle ensembles occurs only when the JNP concentration reaches a minimum threshold (i.e., CMC).³⁴ Figure 3 shows the CD spectra of the JNP10 nanoparticles at varied concentrations in water. It can be seen that at concentrations below 0.025 mg/mL (yellow, blue and magenta curves), the nanoparticles exhibited virtually no PCD absorption, most likely because in these dilute solutions, no nanoparticle ensembles were formed (Figure 1A), and individual nanoparticles were largely PCD-inactive because of plane symmetry. Yet at concentrations higher than 0.05 mg/mL, apparent PCD signals started to emerge and the intensity increased with nanoparticle concentration, indicating that the nanoparticle concentration was sufficiently high for the formation of organized assemblies and the ensembles were optically chiral. For instance, JNP10 nanoparticles showed a broad PCD absorption at 610 nm of +6.1 mdeg at 0.05 mg/mL (green curve), +7.1 mdeg at 0.075 mg/mL (red curve), and +15.2 mdeg at 0.15 mg/mL (black curve). 13 Notably, the PCD intensity observed here with the JNP10 ensembles was ca. 20 times stronger than that of simple nanoparticle dimers, trimers and tetramers reported in earlier studies. 37, 38 This further confirms that the PCD effects were primarily due to the formation of vesicle-like nanostructures by JNP self-assembly. Furthermore, based on the variation of the PCD intensity with nanoparticle concentration, the CMC of the JNP10 nanoparticles can be estimated to be ca. 0.05 mg/mL (0.86 µM), very close to that determined previously by Raman measurements.34

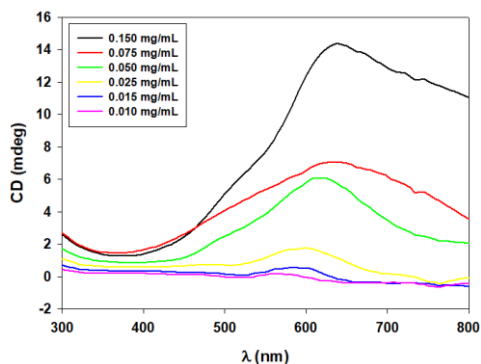
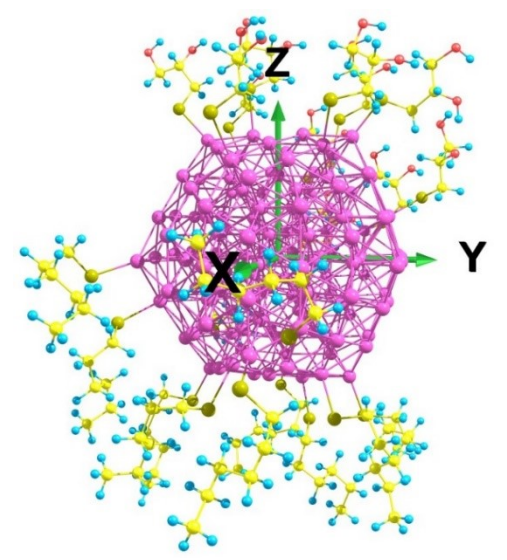


Figure 3. CD spectra of JNP10 nanoparticles at various concentrations in water.

To the best of our knowledge, this is the first ever observation of PCD with hollow nanoparticle ensembles formed by template-less self-assembly. To unravel the microscopic origin of PCD, we carried out first principles calculations of a gold JNP capped with C6 and MPD. Because of asymmetrical distribution of the hydrophobic (C6) and hydrophilic (MPD) ligands, the JNP is anticipated to exhibit a nonzero dipole. Linear response time-dependent density functional theory (TD-DFT) simulations of a Au₂₀ cluster capped with either one or two ligands indeed show a clear ligand-to-metal cluster transition by photoexcitations (**Figures S7-S10**), consistent with results reported previously.³⁹ This suggests that the segregated

distribution of organic capping ligands introduces directionality in the transition dipole moment of the cluster.

We then investigated a more realistic model of the experimental JNPs, as illustrated in **Scheme 1**, where a Au₁₄₇ cluster (dia. 1.6 nm)⁴⁰ was capped with 11 C6 and 11 MPD ligands. Since many more ligands and excited states are involved here, we are interested in a more averaged description for the absorption process. Real time time-dependent density functional tight-binding (TD-DFTB) simulations were carried out. Fourier transforms of the linear response function give the absorption spectra for all excitation transitions of interest. The results (**Figure S11**) show that the absorbance along the *x*-axis was an order of magnitude higher than those along the y- and z-axes. This clearly indicates the average orientation of the transition dipole moment in this range of the spectra (Scheme 1).



Scheme 1. Ground-state geometry of a JNP optimized by DFTB calculations, where a Au_{147} core is capped with 11 C6 and 11 MPD ligands on the two opposite hemispheres.

Thus, the response of a JNP in the visible range can be modelled by an electric (transition) dipole \mathbf{d}_m . For a hollow sphere covered by JNPs, the interaction between any two JNP dipoles is

$$V_{nm} = \frac{1}{gr_{nm}^2} \left[r_{nm}^2 (\boldsymbol{d}_n \cdot \boldsymbol{d}_m) - 3(\boldsymbol{r}_{nm} \cdot \boldsymbol{d}_n) (\boldsymbol{r}_{nm} \cdot \boldsymbol{d}_m) \right] \quad (1)$$

where \mathbf{r}_{nm} is the displacement between particles n and m. The Hamiltonian, $\mathbf{H} = \mathbf{E}\delta_{mn} + \mathbf{V}_{mn}$, can be readily diagonalized, and the eigen states can be expressed in terms of linear combination of ψ_n for an isolated dipole,

$$\Psi_{\mu} = \sum_{n=1}^{N} c_{\mu n} \psi_n \tag{2}$$

The CD strength (R_{μ}) for the μ^{th} state can be calculated from

$$R_{\mu} \propto Re \langle g | \boldsymbol{p} | \mu \rangle \cdot \langle \mu | \boldsymbol{r} \times \boldsymbol{p} | g \rangle$$
 (3)

where g and μ represent the ground state and excited states. Note that as $\langle g|\pmb{p}|\psi_n\rangle \propto \pmb{d}_n$, we can express the CD strength as⁴¹

$$R_{\mu} \propto \sum_{mn} c_{\mu m} c_{\mu n} (\boldsymbol{d}_n \cdot [\boldsymbol{r}_m \times \boldsymbol{d}_m]) \propto \sum_{mn} (\boldsymbol{d}_n \cdot [\boldsymbol{r}_m \times \boldsymbol{d}_m])$$
 (4)

Based on the experimental data (Figure 1B), we consider a hollow sphere with JNPs homogeneously distributed on the surface (**Scheme 2A**). Each Janus particle is considered as a dipole, and the location of the $m^{\rm th}$ dipole is

$$\mathbf{r}_{m} = (\sin\theta_{m}\cos\varphi_{m}, \sin\theta_{m}\sin\varphi_{m}, \cos\theta_{m})^{T} \tag{5}$$

At this point, the three orthogonal unit vectors (Scheme 2A) are

$$\hat{\boldsymbol{r}}_m = \begin{pmatrix} sin\theta_m cos\varphi_m \\ sin\theta_m sin\varphi_m \\ cos\theta_m \end{pmatrix} \quad , \quad \hat{\boldsymbol{\theta}}_m = \begin{pmatrix} cos\theta_m cos\varphi_m \\ cos\theta_m sin\varphi_m \\ -sin\theta_m \end{pmatrix} \quad , \quad \hat{\boldsymbol{\varphi}}_m =$$

$$\begin{pmatrix} -\sin\varphi_m \\ \cos\varphi_m \\ 0 \end{pmatrix} \quad (6)$$

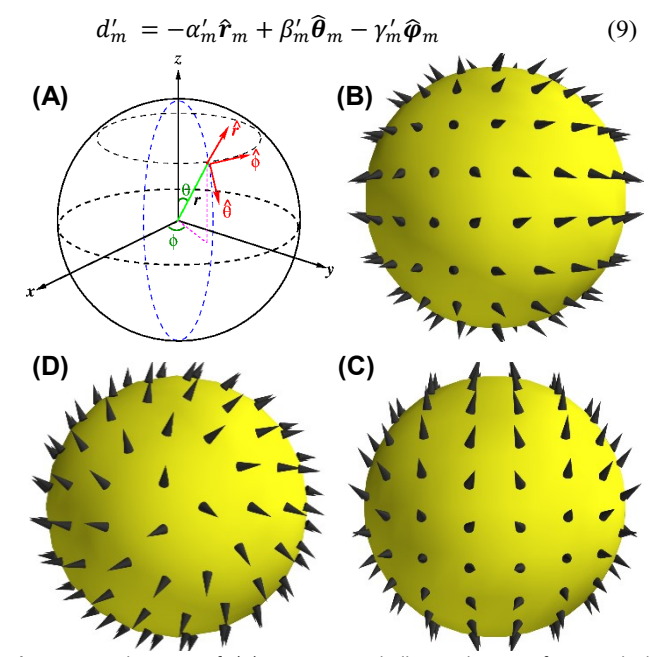
and the dipole \mathbf{d}_{m} can be expressed as a linear combination of these vectors,

$$\boldsymbol{d_m} = \alpha_m \hat{\boldsymbol{r}}_m + \beta_m \hat{\boldsymbol{\theta}}_m + \gamma_m \hat{\boldsymbol{\varphi}}_m \tag{7}$$

Since the dipoles are uniformly distributed, it is reasonable to assume that dipoles exist at both ${\bf r}_m$ and its inversion site, $-{\bf r}_m$. For $-{\bf r}_m$, its polar and azimuthal angles are $\pi-\theta_m$ and $\pi+\phi_m$, respectively. Therefore, at $-{\bf r}_m$, the local unit vectors are

$$\hat{\boldsymbol{r}}_{m}' = -\hat{\boldsymbol{r}}_{m}, \ \widehat{\boldsymbol{\theta}}_{m}' = \widehat{\boldsymbol{\theta}}_{m}, \ \widehat{\boldsymbol{\varphi}}_{m}' = -\widehat{\boldsymbol{\varphi}}_{m}$$
 (8)

and the dipole at $-\boldsymbol{r}_m$ is



Scheme 2. Schematic of (A) JNPs on a hollow sphere surface, and the arrangements of JNP dipoles (represented by black thorns) along the (B) x, (C) y, and (D) z directions.

Now we examine the summation in eq. (4) and separate the points on a half sphere from their inversions,

$$R_{\mu} \propto \sum_{nm}' [\boldsymbol{r}_{m} \cdot (\boldsymbol{d}_{m} \times \boldsymbol{d}_{n}) - \boldsymbol{r}_{m} \cdot (\boldsymbol{d}'_{m} \times \boldsymbol{d}_{n}) + \boldsymbol{r}_{m} \cdot (\boldsymbol{d}_{m} \times \boldsymbol{d}_{m}) + \boldsymbol{r}_{m} \cdot (\boldsymbol{d}_{m} \times \boldsymbol{d}'_{m}) - \boldsymbol{r}_{m} \cdot (\boldsymbol{d}'_{m} \times \boldsymbol{d}'_{n})] = \sum_{nm}' \{ [\boldsymbol{r}_{m} \times (\boldsymbol{d}_{m} - \boldsymbol{d}'_{m})] \cdot (\boldsymbol{d}_{n} + \boldsymbol{d}'_{n}) \}$$

$$(10)$$

where the summation over m and n is limited to the half sphere. Using the relations,

$$\hat{\boldsymbol{r}}_{m} \times \widehat{\boldsymbol{\theta}}_{m} = \widehat{\boldsymbol{\varphi}}_{m}, \hat{\boldsymbol{r}}_{m} \times \widehat{\boldsymbol{\varphi}}_{m} = \widehat{\boldsymbol{\theta}}_{m}$$
(11)

we have

$$R_{\mu} \propto \sum_{nm}^{\prime} \{ [\boldsymbol{r}_{m} \times (\boldsymbol{d}_{m} - \boldsymbol{d}_{m}^{\prime})] \cdot (\boldsymbol{d}_{n} + \boldsymbol{d}_{n}^{\prime}) \} = r_{o} \sum_{nm}^{\prime} [(\alpha_{n} - \alpha_{n}^{\prime}) \boldsymbol{\hat{r}}_{n} + (\beta_{n} + \beta_{n}^{\prime}) \boldsymbol{\hat{\theta}}_{n} + (\gamma_{n} - \gamma_{n}^{\prime}) \boldsymbol{\hat{\varphi}}_{n}] \cdot [(\beta_{m} - \beta_{m}^{\prime}) \boldsymbol{\hat{\theta}}_{m} - (\gamma_{m} + \alpha_{m}^{\prime}) \boldsymbol{\hat{r}}_{n}] \cdot [(\beta_{m} - \beta_{m}^{\prime}) \boldsymbol{\hat{\theta}}_{m} - (\gamma_{m} + \alpha_{m}^{\prime}) \boldsymbol{\hat{r}}_{n}] \cdot [(\beta_{m} - \beta_{m}^{\prime}) \boldsymbol{\hat{\theta}}_{m}] \cdot$$

$$\gamma_m')\widehat{\boldsymbol{\varphi}}_m$$
 (12)

From the above expression, it is clear that to have nonzero chirality R_{μ} , the dipoles cannot be all along $\widehat{\boldsymbol{r}}_m$ and must have components along $\widehat{\boldsymbol{\theta}}_m$ and $\widehat{\boldsymbol{\varphi}}_m$. If we set $\alpha_m=\alpha_m'=\alpha$, i.e., the dipoles tend to point either outward or inward, to have a finite R_{μ} , the simplest solutions are $\beta_m=\beta_m'=\beta$ and $\gamma_m=\gamma_m'=\gamma$, where $\pi<\phi_{\text{m}}<2\pi$ and

$$R_{\mu} \propto -4\beta\gamma \sum_{nm}' [\cos\theta_{n}\cos\theta_{m}\cos(\varphi_{n} - \varphi_{m}) + \sin\theta_{n}\sin\theta_{m}] =$$

$$-4\beta\gamma \sum_{nm}' \sin\theta_{n}\sin\theta_{m}$$
(13)

As $\sin\theta_m$ and $\sin\theta_n$ are always positive, the dipoles along a latitude circle form a vortex-like structure (**Scheme 2B-D**). The fixed sign in β and γ is due to the slightly preferred dipolar orientations between adjacent JNPs.

For monofunctionalized AuC6 and AuMPD nanoparticles, the dipole moment associated with individual nanoparticles is anticipated to be essentially zero; so is the BE nanoparticles. Yet, for AuC6-MPD JNPs, non-zero nanoparticle dipole arises due to the asymmetric segregation of the C6 and MPD ligands, and increases with an increasing number of C6 ligands replaced by MPD on the nanoparticle surface. That is, the dipole moment increases in the order of JNP1 < JNP4 < JNP10. We will establish a quantitative relation between the MPD coverage and the nanoparticle dipole moment. If we arrange the ligands in such a way that the MPD ligands are located in the range of $\theta \in [0, \theta_{\rm o}]$ (Scheme 1), the MPD coverage f is then defined as

$$f = \frac{2\pi R^2 \int_0^{\theta_o} \sin\theta d\theta}{2\pi R^2 \int_0^{\pi} \sin\theta d\theta} = \frac{1}{2} (1 - \cos\theta_o)$$
 (14)

where R is the radius of the nanoparticle. Thus, from the surface coverage f, we can obtain θ_0 . Correspondingly, the C6 ligands will be located in the range of $\theta \in [\theta_0, \pi]$.

Now if we denote the dipole densities in the MPD region and in the C6 regions are p_M and p_C , respectively, the effective dipole

moment of the nanoparticle, which is oriented along the z-axis, is

$$\mathbf{d} = 2\pi R^2 \mathbf{e}_z \int_0^{\pi} p(\theta) \cos\theta \sin\theta d\theta \tag{15}$$

where $p(\theta)$ is dipole density as a function of θ , $p(\theta) = p_M$ for $\theta \in [0, \theta_0]$, and $p(\theta) = p_C$ for $\theta \in [\theta_0, \pi]$, with the ligands assumed to be normal to the nanoparticle surface contributing the $\cos\theta$ factor in eq. (15). Therefore, we have

$$\mathbf{d} = 2\pi R^2 (1 - \cos^2 \theta_0) (p_M - p_C) \tag{16}$$

This expression indicates that at $\theta_o = 0$ or π , i.e., the nanoparticle is fully covered by only one kind of ligands, $\mathbf{d} = 0$.

For a given dipole distribution, the Hamiltonian H = $E\delta_{mn}$ + V_{mn} can then be diagonalized and the CD spectrum can be computed, according to eq. (4). Due to the weak interactions between JNPs, we consider a largely random distribution for the dipole vectors in hollow nanoparticle ensembles, which, however, contains a small portion of a vortex pattern, as depicted above in Scheme 2B-D. To satisfactorily model the experimentally observed CD spectra, we consider a three-level system (two resonant energies). Since the resonant energy E appears only in the diagonal terms in the Hamiltonian, for a given dipole distribution, the eigen values $\delta \mathsf{E}_\mu$ and functions Ψ_μ can be obtained by setting E = 0. Then the eigen values of the system are E_{μ} = E + δE_{μ} and E'_{μ} = E' + δE_{μ} , where E and E' are the two resonant energies of an isolated nanoparticle. In addition, we include the level broadening γ and γ' for the levels associated with E and E'. Finally, the CD signal at frequency $\boldsymbol{\omega}$ is calculated from

$$CD(\omega) = \frac{1}{\pi} \sum_{\mu} R_{\mu} \left[\frac{\gamma}{(\hbar \omega - E_{\mu})^2 + \gamma^2} + \frac{\gamma \gamma}{(\hbar \omega - E_{\mu}')^2 + \gamma^{\prime 2}} \right]$$
(17)

Experimentally, in the self-assembly into vesicle-like, hollow nanostructures, the JNP dipoles are most likely pointed either inward or outward, akin to conventional vesicles formed by surfactant molecules (Figure 1B inset). Therefore, based on eq. (13), this leads to an effective vortex arrangement of the JNP dipoles on the surface of a hollow sphere (Scheme 2) and hence the appearance of PCD signals. In fact, the CD profiles of the three JNP samples can be quantitatively fitted by using eq. (17) at E = 1.25 eV, E' = 1.75 eV, $\gamma = 0.4$ eV, and $\gamma' = 0.58$ eV, as manifested by the dashed curves in Figure 2B. Furthermore, from the MPD coverage f in JNP1, JNP4, and JNP10 (Figure S2), the nanoparticle dipole moment d can also be quantified, according to eq. (14), at 0.578, 0.812, and 0.948 Do, respectively, where Do is the dipole moment of a perfect JNP (i.e., exactly 50% each of C6 and MPD). This is consistent with the enhanced asymmetry (dipole) of the JNPs with an increasing number of polar MPD ligands incorporated onto the nanoparticle surface.

With such remarkable chirality of the vesicle-like nanostructures of JNPs, the hollow interiors can be exploited as a nanoscale vehicle for enantioselective phase transfer of chiral molecules,³² leading to ready separation of optical isomers.⁴²

We used alanine as the illustrating example. Experimentally, JNP10 nanoparticles were dispersed at a concentration of 0.15 mg/mL in CHCl₃ and mixed with aqueous solutions of alanine enantiomers, and the organic nanoparticle layer was monitored by CD measurements. From Figure 4, it can be seen that JNP10 nanoparticles exhibited a PCD profile in CHCl₃ similar to that in H₂O before mixing with alanine (Figures 2 and 3) with a positive peak of +13.9 mdeg at 606 nm, suggesting that both vesicle- and reverse vesicle-like structures of the JNPs followed the same patterns of nanoparticle organization (black curve, Scheme 2). After mixing with L-Ala in water, CD measurements of the CHCl₃ layer showed virtually no change (red curve), indicating a lack of interactions between the JNP10 nanoparticles and L-Ala (peak intensity decreased only slightly to +12.9 mdeg). However, mixing with D-Ala led to a drastic change of the nanoparticle PCD response (green curve), where the CD peak actually became negative (-8.3 mdeg). It has been known that a chiral structure is more likely to interact with molecules of opposite chirality because it provides a better "groove" for the adsorption.⁴² This implies that the chirality of the JNP10 nanoparticle ensembles was equivalent to that of an L enantiomer. In addition, the change of sign of the PCD signals upon interaction with D-Ala is likely due to the physical confinement of the D-Ala molecules within the nanoscale hollow interior of the JNP vesicles, such that they behaved analogously to D-Ala crystals where negative CD absorption is generally observed and may be enhanced by nanoparticle SPR.43

Such a unique property can be exploited for the separation of the D and L enantiomers. In fact, after mixing with a mixture of D- and L-Ala (yellow curve), the PCD profile of the nanoparticle layer resembles that with D-Ala alone, displaying a peak intensity of -4.8 mdeg. This suggests selective interactions of the JNP ensembles with the D enantiomer but not the L counterpart.

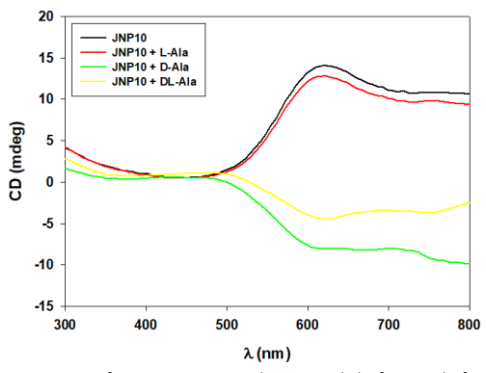


Figure 4. CD spectra of JNP10 nanoparticles in CHCl $_3$ before and after mixing with L-alanine, D-alanine, or D,L-alanine in water. Nanoparticle concentration 0.15 mg/mL and alanine concentration 0.1 M.

3. Conclusion

In summary, AuC6-MPD JNPs were prepared by interfacial ligand exchange reactions of AuC6 nanoparticles with MPD ligands. The resulting JNPs formed (reverse) vesicle-like organized ensembles in water and apolar organic media at sufficiently high concentrations, which exhibited apparent PCD

absorption. The PCD intensity was found to increase with increasing nanoparticle concentration. This was accounted for by the template-less self-assembly of JNP dipoles into a vesiclelike, hollow structure, where a dipole vortex was formed, as manifested in theoretical simulations based on first principles calculations. By contrast, no PCD signals were observed with individual nanoparticles or solid ensembles produced with the bulk-exchange counterparts. Remarkably, the Janus nanoparticle ensembles showed high enantioselectivity towards D-alanine, rather than the L enantiomer, a unique property that may be exploited for nanoparticle-based separation of optical isomers and biosensing.44

4. Experimental Section

Chemicals. Hydrogen tetrachloroauric acid trihydrate (HAuCl₄·3H₂O, Fisher Scientific, 99%), tetra-*n*-octylammonium bromide (TOABr, Alfa Aesar, 98%), 1-hexanethiol (C6SH, Acros, 96%), sodium borohydride (NaBH₄, Acros, 99%), racemic 3mercapto-1, 2-propanediol (MPD, Aldrich, 95%), L-alanine (L-Ala, Acros, 99%), D-alanine (D-Ala, Acros, +99%), and D,Lalanine (D,L-Ala, Acros, 99%) were used as received. All solvents were purchased from commercial sources at their highest purities and used without further treatment. Water was supplied by a Barnstead Nanopure water system (18.3 $M\Omega$ ·cm). Preparation of gold nanoparticles protected by C6SH (AuC6) and MPD (AuMPD) ligands. AuC6 nanoparticles were synthesized by using the Brust method.⁴⁵ In a typical reaction, 30 mL of an aqueous HAuCl₄ solution (0.03 M) was mixed with 20 mL of TOABr in toluene (0.20 M) under vigorous stirring for 1 h. The orange organic phase was then collected, into which was injected 150 µL (1.05 mmol) of C6SH with a micropipette (Accumax Pro) under magnetic stirring, and the solution became colorless. The addition of 24 mL of a chilled aqueous NaBH₄ solution (0.43 M) into the solution led to the rapid appearance of a dark brown color, indicating the formation of gold nanoparticles. The reaction mixture was stirred for 4 h before the organic phase was collected, dried by rotary evaporation, and washed five times with methanol to remove excess C6SH, phase-transfer catalysts, and reaction byproducts. The resulting AuC6 nanoparticles exhibited an average core diameter of 2.7 ± 0.4 nm, as determined by TEM measurements (Figure S1).

AuMPD nanoparticles were prepared in a similar fashion except that an equivalent amount of MPD was used instead of C6SH.

Preparation of AuC6-MPD Janus nanoparticles (JNPs). The synthesis of AuC6-MPD Janus nanoparticles has been detailed previously. 30-32 Briefly, the AuC6 nanoparticles prepared above were dispersed in toluene and deposited onto the water surface of a Langmuir-Blodgett trough (NIMA 611D). After evaporation of the organic solvent, the nanoparticle monolayer was compressed to a desired surface pressure such that the interparticle spacing was less than twice the fully extended chain length of the C6SH ligands. A calculated amount of MPD was then injected into the water subphase using a micropipette to initiate interfacial ligand exchange reactions. The resulting

particles were collected after various reaction times (i.e., 1, 4, or 10 h) so as to vary the concentration of the MPD ligands onto the nanoparticle surface. The nanoparticles were then collected from the water surface and washed by methanol. The resulting Janus nanoparticles were referred to as JNP1, JNP4 and JNP10, respectively.

As a control experiment, ligand exchange reactions were also carried out by simply mixing both the AuC6 nanoparticles and MPD in THF for 10 h, and the resulting sample was denoted as bulk exchange (BE) nanoparticles.

Phase transfer of alanine by JNPs. In a typical experiment, JNP10 was dispersed in chloroform at a concentration of 0.15 mg/mL, and alanine (L-Ala, D-Ala, or D,L-Ala) was dissolved in water at a concentration of 10 mM. The two solutions were mixed under gentle magnetic stirring for 30 min before an aliquot of the CHCl₃ phase was pipetted for CD measurements. Characterization. Transmission electron microscopy (TEM) studies were carried out with a Philips CM300 microscope operated at 300 kV, and atomic force microscopic (AFM) studies were performed with a Molecular Imaging PicoLE SPM instrument. UV-vis absorption spectra were acquired using a PerkinElmer Lambda 35 UV/Vis Spectrometer with a 1 cm quartz cuvette. FTIR measurements were carried out with a PerkinElmer Spectrum One spectrometer. Proton nuclear magnetic resonance (1H NMR) measurements were conducted with a Varian Unity 500 MHz spectrometer with the samples dissolved in deuterated chloroform (CDCl₃). Circular dichroism (CD) measurements were carried out with a JASCO J1500 CD spectrometer using a 1 cm quartz cuvette.

Computational methods. Two models were used in the calculations, one for a small cluster where a more accurate theory was applied, and a large cluster to model the realistic Janus nanoparticle. The small cluster model contained a Au_{20} core and two ligands, i.e., one C6 and one MPD. The larger cluster model contained a Au_{147} core capped with eleven C6 and eleven MPD ligands. This model has approximately the size of the Janus particle used in the experiment.

We performed density function theory (DFT) calculations for the small cluster. The ground state geometry optimization was performed using the hybrid B3LYP functional and the 6-31G* basis set for all elements except for gold atoms where an effective core potential LANL2DZ was used (denoted as B3LYP/6-31G*-LANL2DZ). To investigate the excited electronic state, we applied linear response time-dependent DFT (TD-DFT) method at the CAM-B3LYP/6-31G*-LANL2DZ level of theory. The calculations were carried out using the Q-Chem 5.0 program package.

For the larger model system, the ground state geometry optimization was carried out employing the density functional tight-binding (DFTB) approach and the SK parameters were used as aurog-1-1 in the DFTB+ program. To investigate electronic excited states, we performed real time TD-DFTB method using the lodestar program package. Fourier transform was then used to obtain the absorption spectra.

Conflicts of interest

There are no conflicts to declare.

Acknowledgements

We thank Mr. Y. Peng for the assistance in manuscript preparation. This work was supported in part by the National Science Foundation DMR-1409396 (SC), CHE-1701408 (SC), CHE-1500285 (HW), and the National Natural Science Foundation of China 21673017 (CY), U1530401 (CY). TEM work was performed at the National Center for Electron Microscopy, Lawrence Berkeley National Laboratory, as part of a user project. CD measurements were carried out using the JASCO J1500 CD spectrometer purchased by the NIH S100D016246-01A1 grant. The calculations used the resources of the National Energy Research Scientific Computing Center, a DOE Office of the Science User Facility supported by the Office of Science of the U.S. Department of Energy under Contract No. DE-AC02-05CH11231. Z.G.Y. was supported by the US Army Research Office under contract No. W911NF-17-1-0511.

References

- 1. J. Kumar, K. G. Thomas and L. M. Liz-Marzan, *Chem Commun*, 2016, **52**, 12555-12569.
- W. Ma, L. G. Xu, A. F. de Moura, X. L. Wu, H. Kuang, C. L. Xu and N. A. Kotov, *Chem Rev*, 2017, 117, 8041-8093.
- F. L. Gao, M. Z. Sun, W. Ma, X. L. Wu, L. Q. Liu, H. Kuang and C. L. Xu, Adv Mater, 2017, 29, 1606864.
- 4. B. Ranjbar and P. Gill, Chem Biol Drug Des, 2009, **74**, 101-120.
- N. Berova, L. Di Bari and G. Pescitelli, Chem Soc Rev, 2007, 36, 914-931.
- J. George and K. G. Thomas, J Am Chem Soc, 2010, 132, 2502-2503.
- G. Shemer, O. Krichevski, G. Markovich, T. Molotsky, I. Lubitz and A. B. Kotlyar, J Am Chem Soc, 2006, 128, 11006-11007.
- 8. Z. Y. Fan and A. O. Govorov, *Nano Lett*, 2012, **12**, 3283-3289.
- B. Frank, X. H. Yin, M. Schaferling, J. Zhao, S. M. Hein, P. V. Braun and H. Giessen, Acs Nano, 2013, 7, 6321-6329.
- M. Esposito, V. Tasco, F. Todisco, M. Cuscuna, A. Benedetti, M. Scuderi, G. Nicotra and A. Passaseo, *Nano Lett*, 2016, 16, 5823-5828.
- 11. M. Esposito, V. Tasco, F. Todisco, M. Cuscuna, A. Benedetti, D. Sanvitto and A. Passaseo, *Nat Commun*, 2015, **6**, 6484.
- 12. F. Hidalgo, A. Sanchez-Castillo, I. L. Garzon and C. Noguez, *Eur Phys J D*, 2009, **52**, 179-182.
- C. E. Roman-Velazquez, C. Noguez and I. L. Garzon, J Phys Chem B, 2003, 107, 12035-12038.
- F. Hidalgo, C. Noguez and M. O. de la Cruz, *Nanoscale*, 2014,
 6, 3325-3334.
- 15. A. Sanchez-Castillo, C. Noguez and I. L. Garzon, *J Am Chem Soc*, 2010, **132**, 1504-1505.
- T. G. Schaaff and R. L. Whetten, J Phys Chem B, 2000, 104, 2630-2641.
- 17. M. C. di Gregorio, A. Ben Moshe, E. Tirosh, L. Galantini and G. Markovich, *J Phys Chem C*, 2015, **119**, 17111-17116.
- 18. S. Hou, J. Yan, Z. J. Hu and X. C. Wu, *Chem Commun*, 2016, **52**, 2059-2062.
- 19. M. Z. Sun, L. G. Xu, J. H. Banhg, H. Kuang, S. Alben, N. A. Kotov and C. L. Xu, *Nat Commun*, 2017, **8**, 1847.
- 20. X. Lan and Q. Wang, Adv Mater, 2016, 28, 10499-10507.
- C. C. Rao, Z. G. Wang, N. Li, W. Zhang, X. C. Xu and B. Q. Ding, Nanoscale, 2015, 7, 9147-9152.
- 22. Z. Y. Fan and A. O. Govorov, *Nano Lett*, 2010, **10**, 2580-2587.

- S. H. Jung, J. Jeon, H. Kim, J. Jaworski and J. H. Jung, J Am Chem Soc, 2014, 136, 6446-6452.
- R. Y. Wang, H. L. Wang, X. C. Wu, Y. L. Ji, P. Wang, Y. Qu and T. S. Chung, Soft Matter, 2011, 7, 8370-8375.
- S. Droulias and V. Yannopapas, J Phys Chem C, 2013, 117, 1130-1135.
- J. W. Jarrett, T. Zhao, J. S. Johnson, X. Y. Liu, P. F. Nealey, R. A. Vaia and K. L. Knappenberger, J Phys Chem Lett, 2016, 7, 765-770.
- C. Q. Shen, X. Lan, X. X. Lu, W. H. Ni and Q. B. Wang, *Chem Commun*, 2015, **51**, 13627-13629.
- S. Hou, H. Zhang, J. Yan, Y. L. Ji, T. Wen, W. Q. Liu, Z. J. Hu and X. C. Wu, *Phys Chem Chem Phys*, 2015, 17, 8187-8193.
- X. Jin, J. Jiang and M. H. Liu, Acs Nano, 2016, 10, 11179-11186.
- 30. S. Pradhan, L. P. Xu and S. W. Chen, *Adv Funct Mater*, 2007, **17**, 2385-2392.
- 31. Y. Song, L. M. Klivansky, Y. Liu and S. W. Chen, *Langmuir*, 2011, **27**, 14581-14588.
- 32. Y. Song and S. W. Chen, Langmuir, 2014, 30, 6389-6397.
- 33. Y. Song and S. W. Chen, Chem Asian J, 2014, 9, 418-430.
- 34. Q. Xu, X. W. Kang, R. A. Bogomolni and S. W. Chen, *Langmuir*, 2010, **26**, 14923-14928.
- 35. Y. Yang, S. Matsubara, M. Nogami, J. L. Shi and W. M. Huang, *Nanotechnology*, 2006, **17**, 2821-2827.
- 36. S. K. Ghosh and T. Pal, Chem Rev, 2007, 107, 4797-4862.
- 37. A. O. Govorov, Y. K. Gun'ko, J. M. Slocik, V. A. Gerard, Z. Y. Fan and R. R. Naik, *J Mater Chem*, 2011, **21**, 16806-16818.
- 38. Z. J. Wang, F. Cheng, T. Winsor and Y. M. Liu, Nanotechnology, 2016, 27.
- S. M. Ansar, G. S. Perera, D. P. Jiang, R. A. Holler and D. M. Zhang, *J Phys Chem C*, 2013, 117, 8793-8798.
- M. J. Hostetler, J. E. Wingate, C. J. Zhong, J. E. Harris, R. W. Vachet, M. R. Clark, J. D. Londono, S. J. Green, J. J. Stokes, G. D. Wignall, G. L. Glish, M. D. Porter, N. D. Evans and R. W. Murray, *Langmuir*, 1998, 14, 17-30.
- 41. A. I. Shlykov, A. S. Baimuratov, A. V. Baranov, A. V. Fedorov and I. D. Rukhlenko, *Opt Express*, 2017, **25**, 3811-3825.
- 42. A. J. Gellman, Y. Huang, X. Feng, V. V. Pushkarev, B. Holsclaw and B. S. Mhatre, *J Am Chem Soc*, 2013, **135**, 19208-19214.
- 43. H. Y. Chen, L. Li, D. Liu, H. J. Huang, J. P. Deng and W. T. Yang, RSC Adv, 2014, 4, 63611-63619.
- 44. X. L. Zhao, L. G. Xu, M. Z. Sun, W. Ma, X. L. Wu, C. L. Xu and H. Kuang, *Nat Commun*, 2017, **8**, 2007.
- 45. M. Brust, M. Walker, D. Bethell, D. J. Schiffrin and R. Whyman, *J Chem Soc-Chem Commun*, 1994, 801-802.

TOC Graph

